

SMEFT effects on gravitational wave spectrum from electroweak phase transition

Katsuya Hashino¹, and Daiki Ueda²

¹ *Department of Physics, Faculty of Science and Technology, Tokyo University of Science, Noda, Chiba 278-8510, Japan*

² *Center for High Energy Physics, Peking University, Beijing 100871, China*

E-mail: hashino@rs.tus.ac.jp, ueda@pku.edu.cn

ABSTRACT: Future gravitational wave observations are potentially sensitive to new physics corrections to the Higgs potential once the first-order electroweak phase transition arises. We study the SMEFT dimension-six operator effects on the Higgs potential, where three types of effects are taken into account: (i) SMEFT tree level effect on φ^6 operator, (ii) SMEFT tree level effect on the wave function renormalization of the Higgs field, and (iii) SMEFT top-quark one-loop level effect. The sensitivity of future gravitational wave observations to these effects is numerically calculated by performing a Fisher matrix analysis. We find that the future gravitational wave observations can be sensitive to (ii) and (iii) once the first-order electroweak phase transition arises from (i). The sensitivities of the future gravitational wave observations are also compared with those of future collider experiments.

Contents

1	Introduction	1
2	Formula	3
3	First-order phase transitions in SMEFT	5
3.1	Higgs potential	5
3.2	First-order electroweak phase transition	6
4	GW spectrum and statistical analysis	9
4.1	GW spectrum from first-order phase transition	10
4.2	Statistical analysis in GW experiments	12
5	Numerical results	14
6	Summary	17
A	Sensitivity reach of DECIGO at different bench mark point of bubble wall velocity	18

1 Introduction

The CERN large hadron collider (LHC) has discovered the Higgs boson [1, 2] and measured its properties closely resembling the Standard Model (SM). The discovery of the Higgs boson strengthened the conviction of the SM. However, the shape of the Higgs potential is still unknown, and determining the nature of the electroweak phase transition would be a major scientific goal. In particular, the strongly first-order electroweak phase transition (SFO-EWPT) could provide suitable conditions for achieving the observed baryon asymmetry of the universe (BAU) [3–5] in the electroweak baryogenesis scenario, but the SFO-EWPT in the SM only arises for a Higgs mass $m_h \lesssim 65$ GeV [6–10] well below the measured Higgs mass 125 GeV [11]. In these circumstances, there is growing attention to new physics (NP) effects on the Higgs potential from both theoretical and experimental points of view, but the lack of new particle discoveries at the LHC strengthens the possibility of the NP scale higher than the electroweak symmetry breaking (EWSB) scale.

This situation motivates the effective field theory (EFT) approach to describe the NP effects. The Standard Model Effective Field Theory (SMEFT) [12–15] is one of the actively studied EFTs, and information about the NP effects is transferred to higher-dimensional operators of EFTs consisting of the SM fields. To generate the SFO-EWPT, a considerable amount of literature [16–42] has considered the SMEFT dimension-six φ^6 operator¹. In the context of the electroweak baryogenesis scenario, the

¹In Ref. [43], the validity of the SMEFT description for the SFO-EWPT is questioned.

other SMEFT dimension-six operators [18, 25, 44] are also studied. On the experimental grounds, there is growing interest in the constraints on the SMEFT Wilson coefficients from the current and past experimental data, and future collider experiments, e.g., high-luminosity LHC [45], the International Linear Collider (ILC) [46], the Compact Linear Collider (CLIC) [47], the Future Circular Collider of electrons and positrons (FCC-ee) [48], and the Circular Electron Positron Collider (CEPC) [49]. Furthermore, the SFO-EWPT predicts stochastic background of gravitational waves (GWs), and its spectrum can be peaked around the future interferometer experiment band with milli- to deci-Hertz, such as Laser Interferometer Space Antenna (LISA) [50], DECi-hertz Interferometer Gravitational wave Observatory (DECIGO) [51], and Big-Bang Observer (BBO) [52]. Therefore, the sensitivities of future GW observations to the SMEFT φ^6 operator also have been investigated [19, 20, 27, 28, 31–33, 37, 39–41].

The previous works mainly studied a parameter space to generate a detectable amount of GWs, but they have not quantified how precisely the NP effects can be measured once the GWs are detected. In light of these circumstances, in the previous works of the NP search by the GW observations [53], the method of Fisher matrix analysis was proposed to evaluate the expected sensitivities to NP model parameters. This analysis quantifies how precisely the NP model parameters can be measured by the GWs observations, and it is clarified that the GW observations potentially have higher sensitivities to small deviations of the Higgs potential by the NP effects than the future collider experiments such as the ILC-250. This result naturally leads us to study the sub-dominant SMEFT effects on the Higgs potential and the sensitivities of the GW observations to them.

In this paper, we study the SMEFT dimension-six operator corrections to the Higgs potential and the sensitivities of the GW observations to them. We will focus on three types of the SMEFT dimension-six operator effects: (i) SMEFT tree level effect on φ^6 , (ii) SMEFT tree level effects on the wave function renormalization of the Higgs field, and (iii) SMEFT one-loop top-quark effects. Type (i) dominates the SMEFT effect on the Higgs potential and can achieve the SFO-EWPT. Type (ii) is the tree level effects, but not dominant effects because of the suppression by interference effects with the Higgs self couplings. Type (iii) arises from the loop diagrams and can not dominate the SMEFT effect, but it can be a measurable effect because of the large top Yukawa coupling. Therefore, we focus on a scenario where the SFO-EWPT mainly arises by (i), and the Higgs potential is slightly shifted by (ii) and (iii). We will evaluate the SMEFT effects on the GW spectrum and perform the Fisher matrix analysis to clarify the expected sensitivities of future GW observations to (ii) and (iii).

This paper is organized as follows. In Sec. 2, we provide formulae of the SMEFT dimension-six operator effects on the Higgs potential, and in the following section, we evaluate the SMEFT effects on the SFO-EWPT. In Sec. 4, we summarize formulae of the GW spectrum from the SFO-EWPT and how to evaluate the sensitivities of future GWs observations to the SMEFT effects, e.g., the Fisher matrix analysis. In Sec. 5, the results of numerical calculations are collected. We finish with the summary of the paper in Sec. 6.

2 Formula

The information of the NP particles is transferred to higher-dimensional operators of the SMEFT when the NP scale is higher than the EWSB scale. The SMEFT operators contribute to the Higgs potential and affect the EWPT. In this section, we provide the formulae of the SMEFT dimension-six operator effects on the Higgs potential by taking into account the SMEFT effects on the wave function renormalization of the Higgs field and the SMEFT top-quark effects. The Lagrangian of the SMEFT is defined as [12]

$$\mathcal{L}_{\text{SMEFT}} = \mathcal{L}_{\text{SM}} + \sum_i C_i \mathcal{O}_i, \quad (2.1)$$

where the first term on the right-hand side is the SM Lagrangian, and the second term denotes the higher-dimensional operators consisting of the SM fields. The Lagrangian of Eq. (2.1) is invariant under the SM gauge symmetry, and all the SM particles, e.g., W , Z , H , and t , are dynamical. We consider the SMEFT operators involving Higgs and top-quarks, which contribute to the Higgs potential since the top Yukawa coupling is large. For simplicity, we will restrict this study to CP-conserving interactions. The dimension-six operators relevant to the Higgs potential up to the tree level are

$$\mathcal{O}_{H\Box} = (H^\dagger H)\Box(H^\dagger H), \quad (2.2)$$

$$\mathcal{O}_{HD} = (H^\dagger D^\mu H)^*(H^\dagger D_\mu H), \quad (2.3)$$

$$\mathcal{O}_H = (H^\dagger H)^3, \quad (2.4)$$

where the Higgs field is written in unitary gauge as $\sqrt{2}H^T = (0, \varphi) = (0, v + h)$ with $v = 246$ GeV. The dimension-six operators involving the Higgs fields and top quarks are listed as follows,

$$(\mathcal{O}_{uH})_{ij} = (H^\dagger H)(\bar{q}_i u_j \tilde{H}), \quad (2.5)$$

$$(\mathcal{O}_{Hq}^{(1)})_{ij} = (H^\dagger i \overleftrightarrow{D}_\mu H)(\bar{q}_i \gamma^\mu q_j), \quad (2.6)$$

$$(\mathcal{O}_{Hq}^{(3)})_{ij} = (H^\dagger i \overleftrightarrow{D}_\mu^I H)(\bar{q}_i \tau^I \gamma^\mu q_j), \quad (2.7)$$

$$(\mathcal{O}_{Hu})_{ij} = (H^\dagger i \overleftrightarrow{D}_\mu H)(\bar{u}_i \gamma^\mu u_j), \quad (2.8)$$

with the derivative

$$H^\dagger \overleftrightarrow{D}_\mu^I H = H^\dagger \tau^I D_\mu H - (D_\mu H)^\dagger \tau^I H. \quad (2.9)$$

Here, q is the $SU(2)_L$ quark doublet, u the right-handed up-type quark, quark-flavor indices i, j , an $SU(2)_L$ index I , and τ^I the Pauli matrices.

The Higgs Lagrangian including the SMEFT corrections is defined as

$$\mathcal{L}_\varphi = \frac{1}{2}(\partial_\mu \varphi)^2 - \frac{1}{2}\mu^2 \varphi^2 - \frac{1}{4}\lambda \varphi^4 + \Delta \mathcal{L}_{\text{SMEFT}}, \quad (2.10)$$

where the first, second, and third terms represent the SM renormalizable interactions, and the last term denotes the SMEFT corrections. We summarize the SMEFT corrections to the Higgs Lagrangian for each operator as follows:

- \mathcal{O}_H — Substituting the Higgs field $\sqrt{2}H^T = (0, \varphi)$ into $\mathcal{O}_{H\Box}$ yields the correction at the tree-level as follows,

$$\Delta\mathcal{L}_{\text{SMEFT}} = \frac{1}{8}C_H\varphi^6. \quad (2.11)$$

As studied in Ref. [16–24, 26, 27, 29, 31–37, 39, 42], the φ^6 operator can give rise to the SFO-EWPT and is a dominant SMEFT effect on the Higgs Lagrangian.

- \mathcal{O}_{HD} — This operator yields the correction at the tree level to the Higgs Lagrangian as follows,

$$\Delta\mathcal{L}_{\text{SMEFT}} = \frac{1}{4}C_{HD}\varphi^2(\partial_\mu\varphi)^2. \quad (2.12)$$

As discussed in the next section, Eq. (2.12) contributes to the Higgs potential by the wave function renormalization of φ .

- $\mathcal{O}_{H\Box}$ — This operator yields the correction at the tree level to the Higgs Lagrangian as follows,

$$\Delta\mathcal{L}_{\text{SMEFT}} = -C_{H\Box}\varphi^2(\partial_\mu\varphi)^2. \quad (2.13)$$

Similar to \mathcal{O}_{HD} , Eq. (2.13) contributes to the Higgs potential by the wave function renormalization of φ .

- \mathcal{O}_{uH} — By the top-quark one-loop effects, \mathcal{O}_{uH} generates the corrections to the Higgs Lagrangian as follows,

$$\Delta\mathcal{L}_{\text{SMEFT}} = C_{uH} \cdot \frac{3}{32\pi^2}Y_t \left(14 - 6\ln\frac{m_t^2}{v^2}\right) \cdot \frac{1}{2}\varphi^2(\partial_\mu\varphi)^2 - \Delta V_{c_{uH}}, \quad (2.14)$$

where Y_t is the top Yukawa coupling, m_t is the mass of the top-quark, and

$$\Delta V_{c_{uH}} \equiv -\frac{12}{64\pi^2} \left[m_t^4(\varphi, C_{uH}) \left(\ln\frac{m_t^2(\varphi, C_{uH})}{v^2} - \frac{3}{2} \right) - m_t^4(\varphi, 0) \left(\ln\frac{m_t^2(\varphi, 0)}{v^2} - \frac{3}{2} \right) \right], \quad (2.15)$$

$$= -C_{uH} \cdot \frac{3}{32\pi^2}Y_t^3\varphi^6 \left(-1 + \ln\frac{Y_t^2\varphi^2}{2v^2} \right) + \mathcal{O}(C_{uH}^2). \quad (2.16)$$

with

$$m_t^2(\varphi, C_{uH}) \equiv \left(\frac{Y_t\varphi}{\sqrt{2}} + \frac{C_{uH}\varphi^3}{2\sqrt{2}} \right)^2. \quad (2.17)$$

Here, the $\overline{\text{MS}}$ regularization scheme is adopted, and the results are evaluated at the EWSB scale $v = 246$ GeV. The first term of Eq. (2.14), and Eq. (2.16) are obtained by the fermionic universal one-loop effective action (UOLEA) [54] calculated by the covariant derivative expansion, and they are consistent with the one-loop anomalous dimension matrix for the dimension-six operators of the SMEFT [14]. As shown in Eq. (2.15) and (2.16), we checked that the one-loop Coleman-Weinberg (CW) potential [55] with C_{uH} effect is consistent with the results of the UOLEA up to the first order of C_{uH} . The first term of Eq. (2.14) contributes to the Higgs potential by the wave function renormalization of φ .

- $\mathcal{O}_{Hq}^{(1)}$, $\mathcal{O}_{Hq}^{(3)}$, \mathcal{O}_{Hu} — These operators potentially involve both Higgs fields and top-quark. Since, however, the neutral Higgs field in the derivative of Eq. (2.6), (2.7), and (2.8) cancels, the SMEFT corrections to the Higgs potential can not arise.

3 First-order phase transitions in SMEFT

We consider the EWPT described by the Higgs potential involving the SMEFT effects of Sec. 2 and discuss the conditions for achieving the SFO-EWPT.

3.1 Higgs potential

We summarize the SMEFT effects on the Higgs Lagrangian at zero temperature. Combining Eq. (2.10), (2.11), (2.12), (2.13), and (2.14), we obtain the following Lagrangian:

$$\mathcal{L}_\varphi = c_{\text{kin}} \varphi^2 (\partial_\mu \varphi)^2 + \frac{1}{8} C_H \varphi^6 - \Delta V_{c_{uH}}, \quad (3.1)$$

Here, c_{kin} is defined as

$$c_{\text{kin}} = c_{\text{kin}}^{(0)} + c_{\text{kin}}^{(1)} \cdot \varphi + c_{\text{kin}}^{(2)} \cdot \varphi^2, \quad (3.2)$$

with

$$c_{\text{kin}}^{(0)} = \frac{1}{4} C_{HD} - C_{H\Box} + \frac{1}{2} C_{uH} \cdot \frac{3}{32\pi^2} Y_t \left(14 - 6 \ln \frac{m_t^2}{v^2} \right), \quad (3.3)$$

$$c_{\text{kin}}^{(1)} = \frac{1}{2} C_{uH} \cdot \frac{3}{32\pi^2} Y_t \left(-\frac{28}{v} \right), \quad (3.4)$$

$$c_{\text{kin}}^{(2)} = \frac{1}{2} C_{uH} \cdot \frac{3}{32\pi^2} Y_t \left(\frac{8}{v^2} \right). \quad (3.5)$$

By a field redefinition,

$$\varphi \rightarrow \varphi - \frac{1}{3} c_{\text{kin}}^{(0)} \cdot \varphi^3 - \frac{1}{4} c_{\text{kin}}^{(1)} \cdot \varphi^4 - \frac{1}{5} c_{\text{kin}}^{(2)} \cdot \varphi^5 + \mathcal{O}(c_{\text{kin}}^2), \quad (3.6)$$

we obtain the Higgs Lagrangian as

$$\mathcal{L}_\varphi = \frac{1}{2} (\partial_\mu \varphi)^2 - V, \quad (3.7)$$

with the Higgs potential up to the first order of the Wilson coefficients,

$$V = \frac{1}{2} \mu^2 \varphi^2 + \frac{1}{4} \left(\lambda - \frac{4}{3} c_{\text{kin}}^{(0)} \mu^2 \right) \varphi^4 - \frac{1}{4} c_{\text{kin}}^{(1)} \mu^2 \varphi^5 + \frac{1}{6} \left(-\frac{3}{4} C_H - 2 c_{\text{kin}}^{(0)} \lambda - \frac{6}{5} c_{\text{kin}}^{(2)} \mu^2 \right) \varphi^6 + \Delta V_{c_{uH}}. \quad (3.8)$$

As explained in the next section, in the numerical calculations, the one-loop CW contribution [55] and the thermal corrections of the SM particles are included in Eq. (3.8).

3.2 First-order electroweak phase transition

The EWPT is described by the effective potential with the CW contributions and finite temperature effects:

$$V_{\text{eff}}(\varphi, T) = V + V_{\text{one-loop}} + \Delta V_T + V_T^{\text{ring}}, \quad (3.9)$$

where V is defined in Eq. (3.8). The CW contributions in the effective potential are given by [55],

$$V_{\text{one-loop}} = \sum_i \frac{n_i}{64\pi^2} M_i^4(\varphi) \left(\ln \frac{M_i^2(\varphi)}{v^2} - c_i \right), \quad (3.10)$$

where the $\overline{\text{MS}}$ regularization scheme is adopted, the right-hand side of Eq. (3.10) is evaluated at the EWSB scale $v = 246$ GeV. Here, the index i runs over the Higgs, W , Z , and t , $c_i = 5/6$ ($3/2$) for the gauge boson (other particles), and n_i is the degrees of freedom of particles ($n_\varphi = 1, n_W = 6, n_Z = 3, n_t = -12$). The field-dependent masses are defined as

$$M_\varphi^2(\varphi) \equiv \mu^2 + 3\lambda\varphi^2, \quad (3.11)$$

$$M_i^{2(\text{L,T})}(\varphi) \equiv \frac{\varphi^2}{4} \begin{pmatrix} g^2 & 0 & 0 & 0 \\ 0 & g^2 & 0 & 0 \\ 0 & 0 & g^2 & gg' \\ 0 & 0 & g'g & g'^2 \end{pmatrix}, \quad \text{for } i = W^1, W^2, W^3, B, \quad (3.12)$$

$$M_t^2(\varphi) \equiv m_t^2(\varphi, 0) = \frac{Y_t^2}{2}\varphi^2, \quad (3.13)$$

where superscript L and T represents longitudinal and transverse parts of the gauge bosons, and g' and g are the SM $U(1)$ and $SU(2)$ gauge coupling, respectively. The parameters μ^2 and λ in the Higgs potential are fixed by the following conditions,

$$\partial_\varphi V_{\text{eff}}(\varphi, 0)|_{\varphi=v} = 0, \quad (3.14)$$

$$\partial_\varphi^2 V_{\text{eff}}(\varphi, 0)|_{\varphi=v} = m_h^2, \quad (3.15)$$

where the Higgs mass is $m_h = 125$ GeV. The thermal loop effects in the effective potential [56] are expressed as

$$\Delta V_T = \frac{T^4}{2\pi^2} \left\{ \sum_{i=\varphi, W, Z} n_i \cdot I_B((M_i(\varphi)/T)^2) + n_t \cdot I_F((M_t(\varphi)/T)^2) \right\}. \quad (3.16)$$

where

$$I_B(a_i^2) = \int_0^\infty dx x^2 \ln \left[1 - \exp \left(-\sqrt{x^2 + a_i^2} \right) \right], \quad (3.17)$$

$$I_F(a_i^2) = \int_0^\infty dx x^2 \ln \left[1 + \exp \left(-\sqrt{x^2 + a_i^2} \right) \right], \quad (3.18)$$

with $a_i \equiv M_i(\varphi)/T$. Under the high temperature approximation, these contributions are roughly given by

$$\begin{aligned} I_B(a_i^2) &\rightarrow -\frac{\pi^4}{45} + \frac{\pi^2}{12}a_i^2 - \frac{\pi}{6}(a_i^2)^{3/2} - \frac{a_i^4}{32}\ln\left(\frac{a_i^2}{\alpha_B}\right) + \dots, \\ I_F(a_i^2) &\rightarrow \frac{7\pi^4}{360} - \frac{\pi^2}{24}a_i^2 - \frac{a_i^4}{32}\ln\left(\frac{a_i^2}{\alpha_F}\right) + \dots, \end{aligned} \quad (3.19)$$

where $\ln \alpha_B = 2 \ln 4\pi - 2\gamma_E + 3/2$, $\ln \alpha_F = 2 \ln \pi - 2\gamma_E + 3/2$ and γ_E is Euler constant. To avoid the IR divergence from Matsubara zero-modes of bosons, we add ring diagram contributions [57] to the potential:

$$V_T^{\text{ring}} = \frac{T}{12\pi} \sum_{i=\varphi, W, Z} n_i \left((M_i^2(\varphi, 0))^{3/2} - (M_i^2(\varphi, T))^{3/2} \right), \quad (3.20)$$

where $M_i^2(\varphi, T) = M_i^2(\varphi) + \Pi_i(T)$ and $\Pi_i(T)$ is the thermal self-energy defined as

$$\Pi_\varphi(T) \equiv T^2 \left(\frac{\lambda}{2} + \frac{3g^2}{16} + \frac{g'^2}{16} + \frac{Y_t^2}{4} \right), \quad (3.21)$$

$$\Pi_i^{(L,T)}(T) \equiv \frac{11T^2}{6} a_i^{(L,T)} \begin{pmatrix} g^2 & 0 & 0 & 0 \\ 0 & g^2 & 0 & 0 \\ 0 & 0 & g^2 & 0 \\ 0 & 0 & 0 & g'^2 \end{pmatrix}, \quad \text{for } i = W^1, W^2, W^3, B. \quad (3.22)$$

with $a_i^L = 1$, and $a_i^T = 0$.

The SFO-EWPT is quantified by the ratio v_c/T_c , where the T_c and v_c are determined by the two conditions

$$\partial_\varphi V_{\text{eff}}(\varphi, T_c)|_{\varphi=v_c} = 0, \quad (3.23)$$

$$V_{\text{eff}}(v_c, T_c) = V_{\text{eff}}(0, T_c). \quad (3.24)$$

At the critical temperature T_c , two energetically degenerate minima arise at $\varphi = 0$ and $\varphi = v_c$ and are separated by an energy barrier. The impact of the SMEFT Wilson coefficients on the v_c/T_c is estimated in Figs. 1-3 to clarify parameter spaces where the SFO-EWPT can arise. Here, we defined $C_H \equiv c_H/\Lambda^2$, $C_{uH} \equiv c_{uH}/\Lambda^2$, $C_{HD} \equiv c_{HD}/\Lambda^2$, and $C_{H\Box} \equiv c_{H\Box}/\Lambda^2$. In Figs. 1-3, contours of v_c/T_c are shown on the $\{\Lambda/\sqrt{|c_H|}, c_{uH}/\Lambda^2\}$, $\{\Lambda/\sqrt{|c_H|}, c_{HD}/\Lambda^2\}$, and $\{\Lambda/\sqrt{|c_H|}, c_{H\Box}/\Lambda^2\}$ planes, respectively. We assumed $c_{H\Box} = c_{HD} = 0$, $c_{uH} = c_{H\Box} = 0$ and $c_{uH} = c_{HD} = 0$ for Fig. 1-3, respectively. From Figs. 1-3, it is found that the C_H tree level effect dominates the SFO-EWPT, and the other operators slightly change the Higgs potential.

For ease of understanding the numerical results, we qualitatively discuss the condition for achieving the SFO-EWPT. For simplicity of explanations, we omit $V_{\text{one-loop}}$, V_T^{ring} , and second or higher order corrections for C_{uH} . From Eq. (3.8) and (3.9), the effective potential at zero temperature is calculated as

$$V_{\text{eff}}(\varphi, 0) = \frac{1}{2}a_2\varphi^2 + \frac{1}{4}a_4\varphi^4 + \frac{1}{5}a_5\varphi^5 + \frac{1}{6}a_6\varphi^6, \quad (3.25)$$

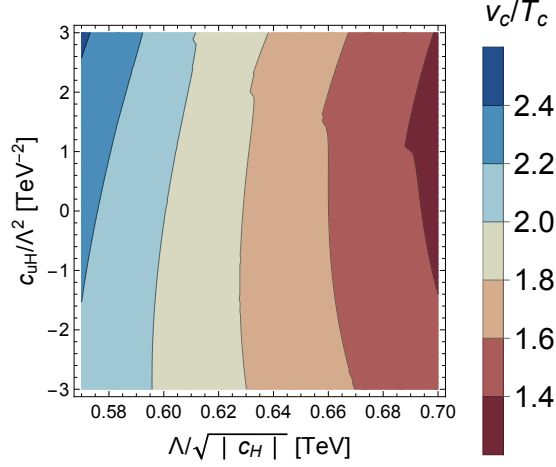


Figure 1. The ratio v_c/T_c as a function of $\Lambda/\sqrt{|c_H|}$ and c_{uH}/Λ^2 . The other Wilson coefficients are taken to be zero, i.e., $c_{H\Box} = c_{HD} = 0$. The region of $v_c/T_c \geq 1$ satisfies the condition for the SFO-EWPT that can produce the GWs.

where

$$\begin{aligned} a_2 &= \mu^2, \quad a_4 = \lambda - \frac{4}{3}c_{\text{kin}}^{(0)}\mu^2, \quad a_5 = -\frac{5}{4}c_{\text{kin}}^{(1)}\mu^2, \\ a_6 &= -\frac{3}{4}C_H - 2c_{\text{kin}}^{(0)}\lambda - \frac{6}{5}c_{\text{kin}}^{(2)}\mu^2 - \frac{9}{16\pi^2}C_{uH}Y_t^3 \left(-1 + \ln \frac{Y_t^2 \varphi^2}{2v^2} \right). \end{aligned} \quad (3.26)$$

The parameters a_2, a_4 , i.e., μ^2 and λ , are fixed by Eq. (3.14) and (3.15) as follows,

$$\partial_\varphi V_{\text{eff}}(\varphi, 0)|_{\varphi=v} = a_2 v + a_4 v^3 + a_5 v^4 + a_6 v^5 = 0, \quad (3.27)$$

$$\partial_\varphi^2 V_{\text{eff}}(\varphi, 0)|_{\varphi=v} = a_2 + 3a_4 v^2 + 4a_5 v^3 + 5a_6 v^4 = m_h^2. \quad (3.28)$$

By solving Eq. (3.27) and (3.28) with respect to the parameters a_2 and a_4 , we obtain

$$V_{\text{eff}}(\varphi, 0) = -\frac{1}{4}(m_h^2 - a_5 v^3 - 2a_6 v^4)\varphi^2 + \frac{1}{4}\left(\frac{m_h^2}{2v^2} - \frac{3}{2}a_5 v - 2a_6 v^2\right)\varphi^4 + \frac{1}{5}a_5 \varphi^5 + \frac{1}{6}a_6 \varphi^6, \quad (3.29)$$

with $a_2 = -(m_h^2 - a_5 v^3 - 2a_6 v^4)/2$, and $a_4 = m_h^2/2v^2 - 3a_5 v/2 - 2a_6 v^2$. For $a_5/2v + a_6 \gtrsim m_h^2/2v^4$ ², both quadratic and quartic terms of the potential at zero temperature change signs, and the SFO-EWPT can happen around the point:

$$\frac{a_5}{2v} + a_6 \sim \frac{m_h^2}{2v^4} \simeq (685 \text{ GeV})^{-2}. \quad (3.30)$$

²More precisely speaking, the quadratic and quartic terms change signs for $a_5/2v + a_6 \gtrsim m_h^2/2v^4$ and $3a_5/2v + 2a_6 \gtrsim m_h^2/2v^4$, respectively.

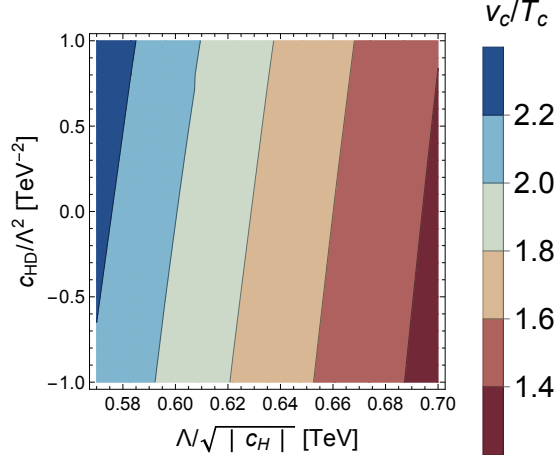


Figure 2. The same plot as Fig. 1 but as a function of $\Lambda/\sqrt{|c_H|}$ and c_{HD}/Λ^2 . $c_{uH} = c_{H\Box} = 0$ is assumed.

Since the \mathcal{O}_H operator dominates the SMEFT effect on the Higgs potential, C_H takes a negative value for the SFO-EWPT. Note here that the origin of the potential becomes a true minimum at zero temperature when C_H is too large. As studied in detail in Ref. [58], the SFO-EWPT where percolation can be possible corresponds to $\Lambda/\sqrt{|c_H|} > 0.55$ TeV. Including the finite temperature effects, the effective Higgs potential in the high-temperature limit of Eq. (3.19) is approximately given by

$$V_{\text{eff}}(\varphi, T) \sim \frac{1}{2}A_2\varphi^2 - \frac{1}{2\sqrt{2}}ET\varphi^3 + \frac{1}{4}A_4\varphi^4, \quad (3.31)$$

where A_2 is a coefficient of the quadratic term involving the thermal corrections, E denotes a coefficient of the cubic term from the thermal effects of the SM bosons, and $A_4 \equiv a_4 + 4a_5\varphi/5 + 2a_6\varphi^2/3$. From Eq. (3.23) and (3.24), the T_c and v_c are calculated as follows,

$$\frac{v_c}{T_c} = \frac{E}{\sqrt{2}A_4} \sim \frac{E}{\sqrt{2}(m_h^2/(2v^2) - 3a_5v/2 - 2a_6v^2)}. \quad (3.32)$$

Therefore, the SFO-EWPT requires $v_c/T_c \geq 1$, i.e., $a_5/2v + a_6 \gtrsim m_h^2/2v^4$. Since a_5 is generated by top-quark loop effects and is a sub-dominant effect, from Eq. (3.32), it is clear that the parameter a_6 , i.e., C_H , dominates the SMEFT effects on v_c/T_c , as shown in Figs. 1-3.

4 GW spectrum and statistical analysis

The GWs can arise from the SFO-EWPT, and their spectrum can be determined by a few quantities, such as the latent heat and the bubble nucleation rate. As explained later, the produced GW spectrum is characterized by four parameters, and the Wilson coefficients of the SMEFT are encoded into the four parameters. Future GW experiments such as LISA, DECIGO, and BBO are potentially sensitive to the GW spectrum from the SFO-EWPT, and the Wilson coefficients of the SMEFT may be constrained. In this section, we summarize the GW spectrum from the SFO-EWPT and analysis to derive the constraints on the Wilson coefficients.

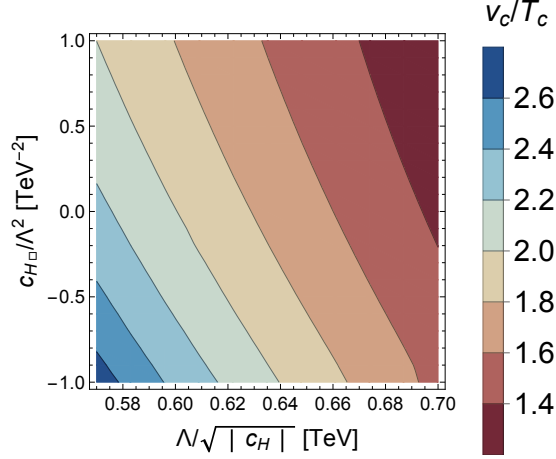


Figure 3. The same plot as Fig. 1 but as a function of $\Lambda/\sqrt{|c_H|}$ and $c_{H\Box}/\Lambda^2$. $c_{uH} = c_{HD} = 0$ is assumed.

4.1 GW spectrum from first-order phase transition

The GW from the first-order phase transition is mainly characterized by four parameters: T_t , α , β/H , and v_b . We refer to these parameters as the phase transition parameters. T_t is the temperature during bubble percolation for the phase transition to complete and is defined by

$$\Gamma/H^4|_{T=T_t} = 1, \quad (4.1)$$

where $H = 8\pi^3 g_* T^4 / 90 m_{\text{Pl}}^2$ is the Hubble parameter in a radiation-dominated epoch with the Plank mass m_{Pl} and degrees of freedom in the plasma $g_* = 106.75$, and Γ is a bubble nucleation rate per unit volume and unit time:

$$\Gamma \simeq T^4 \left(\frac{S_3}{2\pi T} \right)^{3/2} \exp(-S_3/T), \quad (4.2)$$

with a 3-dimensional Euclidean action S_3 , i.e., $O(3)$ symmetric bounce solution. In the numerical calculation, the bounce solution is calculated by the AnyBubble [59] package. Combining Eq. (4.1) and (4.2), T_t is numerically calculated. The second parameter α is a ratio of the released latent heat ϵ and the background plasma energy density $\rho_{\text{rad}}(T) = (\pi^2/30)g_* T^4$ at $T = T_t$ as follows,

$$\alpha \equiv \epsilon(T_t)/\rho_{\text{rad}}(T_t). \quad (4.3)$$

Here, the released latent heat is defined as

$$\epsilon(T) = \Delta V_{\text{eff}} - T \frac{\partial \Delta V_{\text{eff}}}{\partial T}, \quad \Delta V_{\text{eff}} = V_{\text{eff}}(\varphi_-(T), T) - V_{\text{eff}}(\varphi_+(T), T), \quad (4.4)$$

where V_{eff} is defined in Eq. (3.9), and φ_+ and φ_- denote the order parameters for the broken and unbroken phases, respectively. The third parameter β/H represents the inverse of the duration of the

phase transition and is defined as

$$\frac{\beta}{H} \equiv T_t \frac{d}{dT} \left(\frac{S_3}{T} \right) \Big|_{T=T_t}. \quad (4.5)$$

The last parameter v_b is the bubble wall velocity, which is the speed of the bubble wall in the rest frame of the plasma far from the wall. In the following numerical analysis, we choose a benchmark point of $v_b = 0.3$, where the electroweak baryogenesis involving C_{uH} is also possible [18]. In Appendix A, a different choice of the benchmark point of v_b is considered.

The GW from the first-order phase transition arises from three sources: bubble collision, plasma turbulence, and compression wave of plasma. In particular, the compression wave of plasma is the dominant source of the GW spectrum, so we focus only on it in the following numerical calculations. The fitting function for the numerical simulations of the GW spectrum generated by a phase transition during the radiation era is expressed as [60–62]

$$\Omega_{\text{comp}}(f) = 2.061 F_{\text{gw},0} \tilde{\Omega}_{\text{gw}} \left(\frac{f}{\tilde{f}_{\text{comp}}} \right)^3 \left(\frac{7}{4 + 3(f/\tilde{f}_{\text{comp}})^2} \right)^{7/2} \times \begin{cases} \left(\frac{\kappa_v \alpha}{1+\alpha} \right)^2 (H_* R_*)^2, & \text{for } H_* R_* \leq \sqrt{\frac{3}{4} \kappa_v \alpha / (1+\alpha)} \\ \left(\frac{\kappa_v \alpha}{1+\alpha} \right)^{3/2} (H(T_t) R_*)^2, & \text{for } \sqrt{\frac{3}{4} \kappa_v \alpha / (1+\alpha)} < H_* R_* \end{cases} \quad (4.6)$$

where an efficiency factor κ_v [63] is given by a function of α and v_b as follows,

$$\kappa_v(v_b, \alpha) \simeq \begin{cases} \frac{c_s^{11/5} \kappa_A \kappa_B}{(c_s^{11/5} - v_b^{11/5}) \kappa_B + v_b c_s^{6/5} \kappa_A} & \text{for } v_b \lesssim c_s \\ \kappa_B + (v_b - c_s) \delta \kappa + \frac{(v_b - c_s)^3}{(v_J - c_s)^3} [\kappa_C - \kappa_B - (v_J - c_s) \delta \kappa] & \text{for } c_s < v_b < v_J, \\ \frac{(v_J - 1)^3 v_J^{5/2} v_b^{-5/2} \kappa_C \kappa_D}{[(v_J - 1)^3 - (v_b - 1)^3] v_J^{5/2} \kappa_C + (v_b - 1)^3 \kappa_D} & \text{for } v_J \lesssim v_b \end{cases} \quad (4.7)$$

where

$$\kappa_A \simeq v_b^{6/5} \frac{6.9\alpha}{1.36 - 0.037\sqrt{\alpha} + \alpha}, \quad \kappa_B \simeq \frac{\alpha^{2/5}}{0.017 + (0.997 + \alpha)^{2/5}}, \\ \kappa_C \simeq \frac{\sqrt{\alpha}}{0.135 + \sqrt{0.98 + \alpha}}, \quad \kappa_D \simeq \frac{\alpha}{0.73 + 0.083\sqrt{\alpha} + \alpha}. \quad (4.8)$$

Here, c_s is the velocity of sound ($c_s = 0.577$), and

$$v_J = \frac{\sqrt{2/3\alpha + \alpha^2} + \sqrt{1/3}}{1 + \alpha}, \quad \delta \kappa \simeq -0.9 \ln \frac{\sqrt{\alpha}}{1 + \sqrt{\alpha}}. \quad (4.9)$$

Also, $F_{\text{gw},0} = 3.57 \times 10^{-5} (100/g_*)^{1/3}$, $\tilde{\Omega}_{\text{gw}} = 1.2 \times 10^{-2}$, $H_* R_* = (8\pi)^{1/3} (\beta/H)^{-1} \max(c_s, v_b)$ and \tilde{f}_{comp} is the peak frequency given by

$$\tilde{f}_{\text{comp}} \simeq 2.6 \left(\frac{H_* R_*}{1000} \right)^{-1} \left(\frac{T_t}{100 \text{ GeV}} \right) \left(\frac{g_*}{100} \right)^{1/6} 10^{-2} \text{ Hz} \quad (4.10)$$

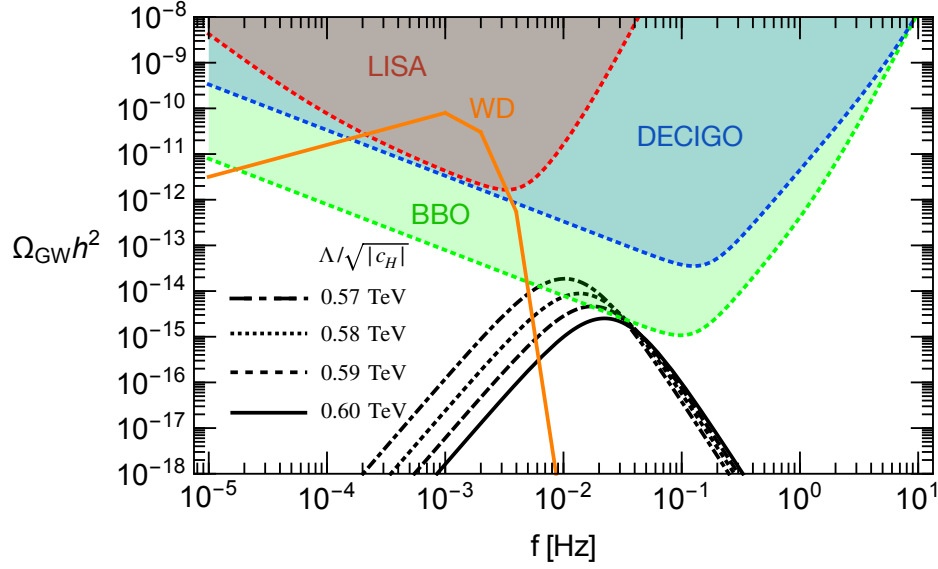


Figure 4. The GW spectra from the SFO-EWPT by the SMEFT \mathcal{O}_H operator effects. The black curves correspond to $\Lambda/\sqrt{|c_H|} = 0.57$ TeV (dot-dashed), 0.58 TeV (dotted), 0.59 TeV (dashed), and 0.60 TeV (solid), respectively, assuming $c_{HD} = c_{H\Box} = c_{uH} = 0$. The colored regions represent the sensitivity regions of LISA (red), DECIGO (blue), and BBO (green). The orange curve denotes a foreground coming from compact white dwarf binaries in our Galaxy.

As explained in the previous sections, the Wilson coefficients of the SMEFT contribute to the effective Higgs potential, and the SMEFT effects are encoded into the phase transition parameters. The point is that the GW spectrum from the first-order phase transition is determined from the Wilson coefficients through the phase transition parameters.

4.2 Statistical analysis in GW experiments

The Wilson coefficients of the SMEFT are potentially measured by future GW observations. The error of the Wilson coefficients denotes room for the NP effects when its central value is zero consistently within the error. We evaluate the confidence interval of the Wilson coefficients in the GW observation by the Fisher matrix analysis and investigate the sensitivity of future GW experiments to the SMEFT operators. The sensitivity of future GW experiments to the Wilson coefficient is well characterized by the signal-to-noise ratio (SNR). The SNR for the observation of GW spectrum is obtained as [51, 53]

$$\text{SNR} = \sqrt{\delta \times T_{\text{obs}} \int_0^\infty df \left[\frac{\Omega_{\text{GW}}(f)}{\Omega_{\text{sen}}(f)} \right]^2}, \quad (4.11)$$

where $\Omega_{\text{GW}} \simeq \Omega_{\text{comp}}$, T_{obs} is the observation period, $\Omega_{\text{sen}} \equiv (2\pi^2 f^3 / 3H_0^2) \cdot S_{\text{eff}}(f)$ is the sensitivity of experiments, which are summarized later, and δ is the number of independent channels for the experiments, i.e., $\delta = 2$ for cross-correlated detectors such as DECIGO and BBO, and $\delta = 1$ for

LISA. The logarithm of the likelihood function is approximated to [51, 53]

$$\delta\chi^2(\{p\}, \{\hat{p}\}) \simeq \mathcal{F}_{ab}(p_a - \hat{p}_a)(p_b - \hat{p}_b), \quad (4.12)$$

where the parameter set $\{p\}$ denotes the Wilson coefficients of the SMEFT, $\{\hat{p}\}$ is the set of fiducial values of $\{p\}$, and \mathcal{F}_{ab} represents the Fisher information matrix [51] defined as follows,

$$\mathcal{F}_{ab} = 2T_{\text{obs}} \int_0^\infty df \frac{\partial_{p_a} S_h(f, \{\hat{p}\}) \partial_{p_b} S_h(f, \{\hat{p}\})}{[S_{\text{eff}}(f) + S_h(f, \{\hat{p}\})]^2}, \quad (4.13)$$

with the power spectrum

$$S_h(f) = \frac{3H_0^2}{2\pi^2} \frac{1}{f^3} \Omega_{\text{GW}}(f). \quad (4.14)$$

Throughout this work, we evaluate the confidence intervals on two-dimensional planes and consider three parameter sets: $\{C_H, C_{uH}\}$, $\{C_H, C_{HD}\}$, and $\{C_H, C_{H\Box}\}$. The 95% C.L. interval of the Wilson coefficients denotes a contour of $\delta\chi^2 = 6.0$ in the two-dimensional plane. The effective sensitivities of each experiment are evaluated as [64, 65]

- LISA

$$S_{\text{eff}}(f) = \frac{20}{3} \frac{4S_{\text{acc}}(f) + S_{\text{sn}}(f) + S_{\text{omn}}(f)}{L^2} \left[1 + \left(\frac{f}{0.41c/2L} \right)^2 \right], \quad (4.15)$$

with $L = 5 \times 10^9$ m and,

$$S_{\text{acc}}(f) = 9 \times 10^{-30} \frac{1}{(2\pi f/1\text{Hz})^4} \left(1 + \frac{10^{-4}}{f/1\text{Hz}} \right) \text{m}^2\text{Hz}^{-1}, \quad (4.16)$$

$$S_{\text{sn}}(f) = 2.96 \times 10^{-23} \text{m}^2\text{Hz}^{-1}, \quad (4.17)$$

$$S_{\text{omn}}(f) = 2.65 \times 10^{-23} \text{m}^2\text{Hz}^{-1}. \quad (4.18)$$

- DECIGO

$$S_{\text{eff}}(f) = \left[7.05 \times 10^{-48} [1 + (f/f_p)^2] + 4.8 \times 10^{-51} \frac{(f/1\text{Hz})^{-4}}{1 + (f/f_p)^2} + 5.33 \times 10^{-52} (f/1\text{Hz})^{-4} \right] \text{Hz}^{-1}, \quad (4.19)$$

with $f_p = 7.36$ Hz.

- BBO

$$S_{\text{eff}}(f) = [2.00 \times 10^{-49} (f/1\text{Hz})^2 + 4.58 \times 10^{-49} + 1.26 \times 10^{-52} (f/1\text{Hz})^{-4}] \text{Hz}^{-1}. \quad (4.20)$$

It is known that the stochastic GWs from astrophysical sources can be a foreground. In our numerical calculations, we add a foreground from compact white dwarf binaries in our Galaxy in the milli-Hertz regime to the effective sensitivity of each experiment. The noise spectrum of the white dwarf is evaluated as [65]

$$S'_{\text{WD}}(f) = \begin{cases} (20/3)(f/1 \text{ Hz})^{-2.3} \times 10^{-44.62} \text{ Hz}^{-1} & \equiv S_{\text{WD}}^{(1)}(f) & (10^{-5} \text{ Hz} < f < 10^{-3} \text{ Hz}), \\ (20/3)(f/1 \text{ Hz})^{-4.4} \times 10^{-50.92} \text{ Hz}^{-1} & \equiv S_{\text{WD}}^{(2)}(f) & (10^{-3} \text{ Hz} < f < 10^{-2.7} \text{ Hz}), \\ (20/3)(f/1 \text{ Hz})^{-8.8} \times 10^{-62.8} \text{ Hz}^{-1} & \equiv S_{\text{WD}}^{(3)}(f) & (10^{-2.7} \text{ Hz} < f < 10^{-2.4} \text{ Hz}), \\ (20/3)(f/1 \text{ Hz})^{-20.0} \times 10^{-89.68} \text{ Hz}^{-1} & \equiv S_{\text{WD}}^{(4)}(f) & (10^{-2.4} \text{ Hz} < f < 10^{-2} \text{ Hz}). \end{cases} \quad (4.21)$$

In the numerical calculations, we adopt the following noise spectrum

$$S_{\text{WD}}(f) = \frac{1}{1/S_{\text{WD}}^{(1)}(f) + 1/S_{\text{WD}}^{(2)}(f) + 1/S_{\text{WD}}^{(3)}(f) + 1/S_{\text{WD}}^{(4)}(f)}. \quad (4.22)$$

In Fig. 4, the sensitivity regions for LISA, DECIGO, and BBO are shown as red-shaded, blue-shaded, and green-shaded regions, respectively. The orange curve denotes the noise spectrum of the white dwarf.

5 Numerical results

Figs. 1-3 show numerical results of ratio v_c/T_c as functions of $\{\Lambda/\sqrt{|c_H|}, c_{uH}/\Lambda^2\}$, $\{\Lambda/\sqrt{|c_H|}, c_{HD}/\Lambda^2\}$, and $\{\Lambda/\sqrt{|c_H|}, c_{H\Box}/\Lambda^2\}$, respectively. We assumed $c_{H\Box} = c_{HD} = 0$, $c_{uH} = c_{H\Box} = 0$, and $c_{uH} = c_{HD} = 0$ for Figs. 1-3, respectively. For all figures, v_c/T_c is larger than one in the regions $\Lambda/\sqrt{|c_H|} \lesssim 0.7 \text{ TeV}$, and the GWs can arise from the SFO-EWPT. Fig. 4 shows the GW spectrum from the SFO-EWPT achieved by the SMEFT operator \mathcal{O}_H . The $\Lambda/\sqrt{|c_H|}$ dependence of the GW spectrum are shown, and the four black curves correspond to $\Lambda/\sqrt{|c_H|} = 0.57 \text{ TeV}$ (dot-dashed), 0.58 TeV (dotted), 0.59 TeV (dashed), and 0.60 TeV (solid). The colored shaded regions represent the effective sensitivities $(2\pi^2 f^3/3H_0^2) \cdot S_{\text{eff}}(f)$ of LISA (red), DECIGO (blue), and BBO (green). The orange curve corresponds to the foreground from compact white dwarf binaries in our Galaxy in the milli-Hertz regime.

We numerically evaluated the three SMEFT operators \mathcal{O}_{uH} , $\mathcal{O}_{H\Box}$, and \mathcal{O}_{HD} effects on the GWs produced by \mathcal{O}_H . To quantitatively evaluate the sensitivity of the future GW experiments to the three SMEFT operator effects, we calculated the SNRs of LISA, DECIGO, and BBO with $T_{\text{obs}} = 1\text{-year}$ statistics and $v_b = 0.3$, as shown in Figs. 5-7 on the $\{\Lambda/\sqrt{|c_H|}, c_{uH}/\Lambda^2\}$, $\{\Lambda/\sqrt{|c_H|}, c_{HD}/\Lambda^2\}$, and $\{\Lambda/\sqrt{|c_H|}, c_{H\Box}/\Lambda^2\}$ planes, respectively. We assumed $c_{H\Box} = c_{HD} = 0$, $c_{uH} = c_{H\Box} = 0$, and $c_{uH} = c_{HD} = 0$ for Figs. 5-7, respectively. In all figures of the LISA experiment, the SNRs for $c_{uH} = c_{H\Box} = c_{HD} = 0$ are smaller than ~ 10 , which corresponds to a typical value for the precisely measurable c_{uH} , $c_{H\Box}$, and c_{HD} as explained later. In the DECIGO experiment under the condition $c_{uH} = c_{H\Box} = c_{HD} = 0$, the SNR of Figs. 5-7 is larger than ~ 10 for $\Lambda/\sqrt{|c_H|} \lesssim 0.64 \text{ TeV}$. The SNR of BBO is ~ 10 times larger than that of DECIGO; see Fig. 4. In Fig. 7, the measurable GWs

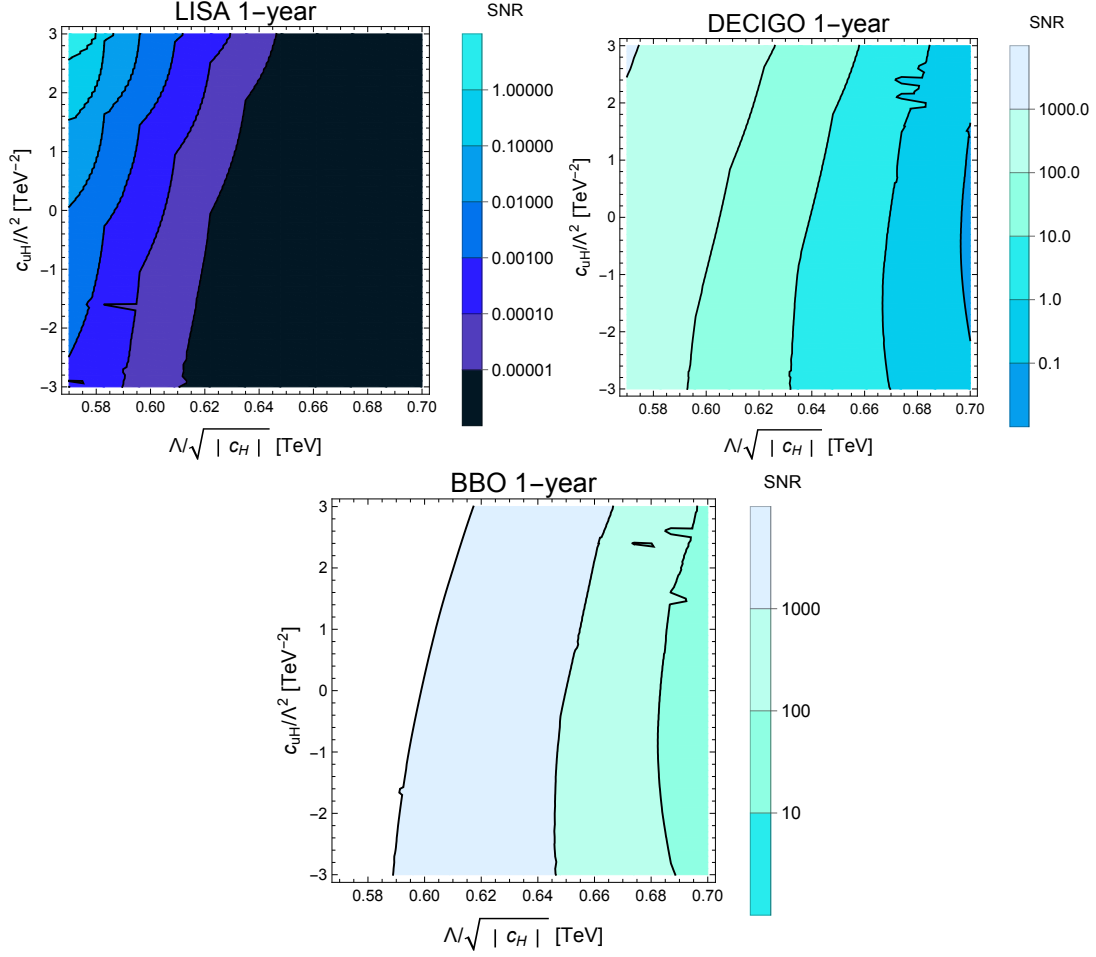


Figure 5. The SNR of the future GW experiments on the $(\Lambda/\sqrt{|c_H|}, c_{uH}/\Lambda^2)$ plane, assuming $v_b = 0.3$, $c_{H\Box} = c_{HD} = 0$, and 1-year statistics at LISA (upper left), DECIGO (upper right), and BBO (bottom). The solid curves denote the contours of SNR.

are not generated in the white-shaded regions. This is because, in the small $\Lambda/\sqrt{|c_H|}$ and $c_{H\Box}/\Lambda^2$ region, a_6 is too large to yield the SFO-EWPT, and in the large $\Lambda/\sqrt{|c_H|}$ and $c_{H\Box}/\Lambda^2$ region, a_6 is too small to yield the SFO-EWPT involving the measurable GWs; see Fig. 3. Comparing Figs. 1-3 with Figs. 5-7, it is found that the behaviors of the contours of SNR are similar to those of v_c/T_c . This is because the phase transition parameters highly depend on v_c/T_c , e.g., $\alpha \propto (v_c/T_c)^2$ [63].

We evaluate the confidence intervals in future GW experiments for the SMEFT Wilson coefficients by performing the Fisher matrix analysis. Figs. 8-10 show the 95% confidence intervals, i.e., $\delta\chi^2 = 6.0$ in Eq. (4.12), in the DECIGO and BBO experiments with $T_{\text{obs}} = 1$ -year statistics and $v_b = 0.3$ for the SMEFT Wilson coefficients C_{uH} , $C_{H\Box}$, C_{HD} , and C_H . In the right panels of Figs. 8-10, the 95% confidence intervals are shown on the $\{c_{uH}/\Lambda^2, \Lambda/\sqrt{|c_H|}\}$, $\{c_{HD}/\Lambda^2, \Lambda/\sqrt{|c_H|}\}$, and $\{c_{H\Box}/\Lambda^2, \Lambda/\sqrt{|c_H|}\}$ planes, respectively. We assumed the central values in the right panels of Figs. 8-10 as $\{c_{uH}/\Lambda^2 = 0, \Lambda/\sqrt{|c_H|} = 0.60 \text{ TeV}\}$, $\{c_{HD}/\Lambda^2 = 0, \Lambda/\sqrt{|c_H|} = 0.60 \text{ TeV}\}$, and

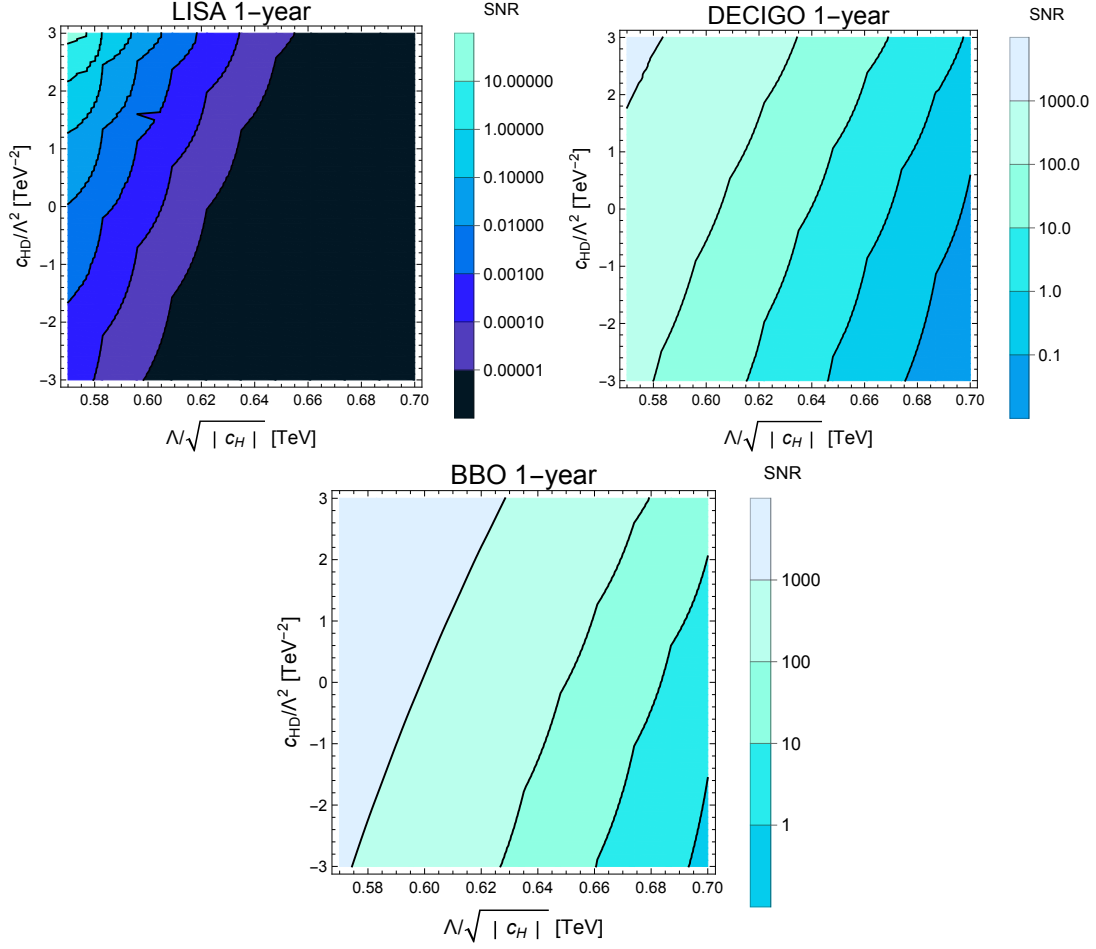


Figure 6. The same plot as Fig. 5 but on the $(\Lambda/\sqrt{|c_H|}, c_{HD}/\Lambda^2)$ plane, assuming $c_{uH} = c_{H\Box} = 0$.

$\{c_{H\Box}/\Lambda^2 = 0, \Lambda/\sqrt{|c_H|} = 0.60 \text{ TeV}\}$, respectively. The shaded blue and red regions denote the 95% confidence regions in the DECIGO and BBO experiments, respectively. The confidence intervals for c_{uH}/Λ^2 , c_{HD}/Λ^2 , and $c_{H\Box}/\Lambda^2$ directions represent allowed NP effects because their central values are assumed to be zero. The dotted blue lines denote the sensitivity reach of the ILC-250 at 95% C.L. [66, 67]. From Figs. 8-10, it is found that the sensitivity of the future GW observations may be higher than that of the future collider experiment. The left panels of Figs. 8-10 show the sensitivity reach of the DECIGO and BBO experiments to $\Lambda/\sqrt{|c_{uH}|}$, $\Lambda/\sqrt{|c_{HD}|}$, and $\Lambda/\sqrt{|c_{H\Box}|}$ as a function of the central values of $\Lambda/\sqrt{|c_H|}$, respectively. We assumed the central values in the left panels of Figs. 8-10 as $c_{uH} = c_{HD} = c_{H\Box} = 0$. The black and red curves correspond to the DECIGO and BBO experiments with $T_{\text{obs}} = 1\text{-year}$ statistics and $v_b = 0.3$, respectively. Each point denotes the magnitude of 95 % confidence intervals for $\Lambda/\sqrt{|c_{uH}|}$, $\Lambda/\sqrt{|c_{HD}|}$, and $\Lambda/\sqrt{|c_{H\Box}|}$ directions. The dotted blue lines are the sensitivity reach of the ILC-250 at 95% C.L. [66, 67], and the dotted red lines are the current bounds at 95% C.L. [68]. Comparing Figs. 5-7 with Figs. 8-10, the sensitivity reach of the

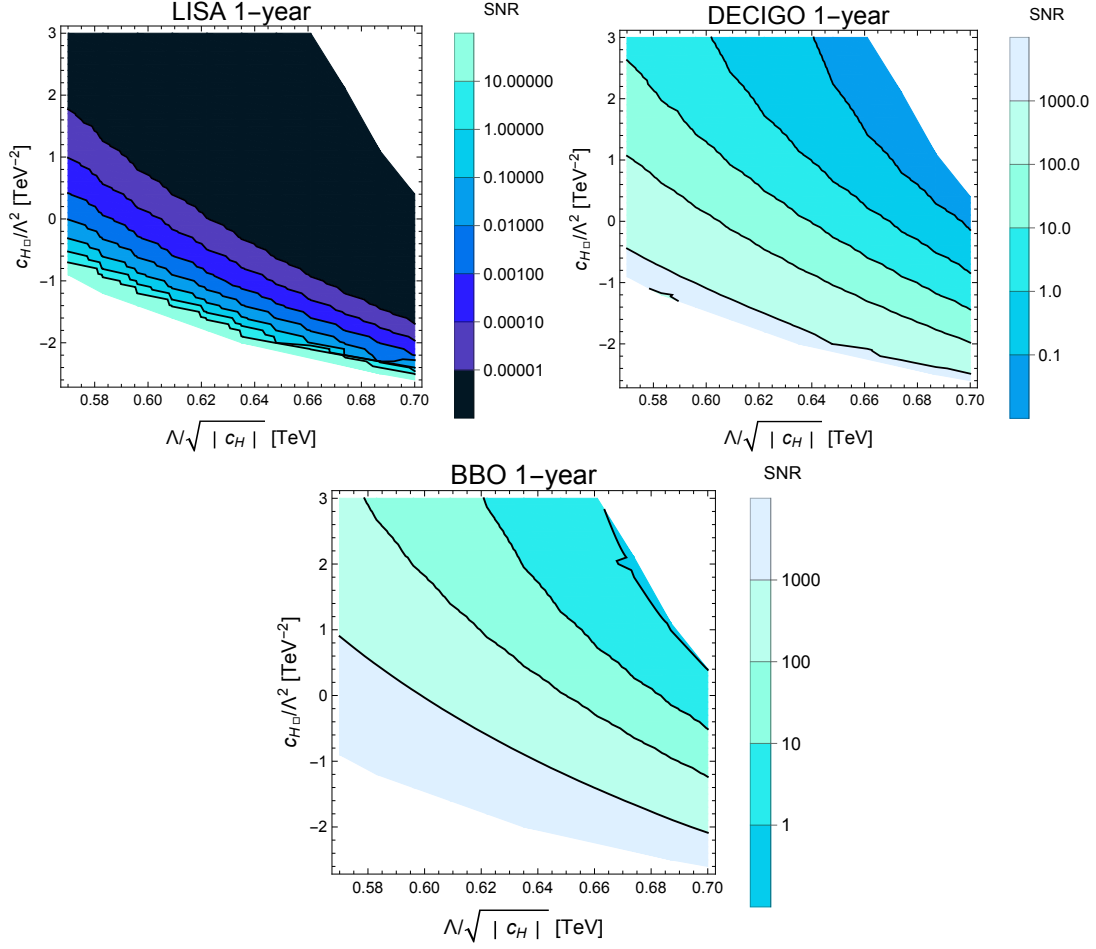


Figure 7. The same plot as Fig. 5 but on the $(\Lambda/\sqrt{|c_H|}, c_{H\Box}/\Lambda^2)$ plane, assuming $c_{uH} = c_{HD} = 0$.

DECIGO and BBO experiments denotes ~ 1 TeV for $\text{SNR} \sim 10$, which denotes a typical value for the precisely measurable c_{uH} , $c_{H\Box}$, and c_{HD} . It is found that the sensitivity reach of the DECIGO and BBO experiments may exceed that of future collider experiments when the SFO-EWPT arises by SMEFT \mathcal{O}_H operators.

6 Summary

We studied the SMEFT dimension-six operator effects on the spectrum of GWs produced from the SFO-EWPT. The three types of the SMEFT operator effects, i.e., (i) \mathcal{O}_H operator tree level effects, (ii) $\mathcal{O}_{H\Box}$ and \mathcal{O}_{HD} operators tree level effects on the wave function renormalization of the Higgs field, and (iii) \mathcal{O}_{uH} operator one-loop level effects were considered. Firstly, we provided formulae of the SMEFT effects on the Higgs potential and calculated v_c/T_c as functions of the three types of SMEFT operators, as shown in Figs. 1-3. We focused on the scenario where the GWs mainly arises by (i), and the GW spectrum is slightly shifted by (ii) and (iii) because (i) is the dominant effect on

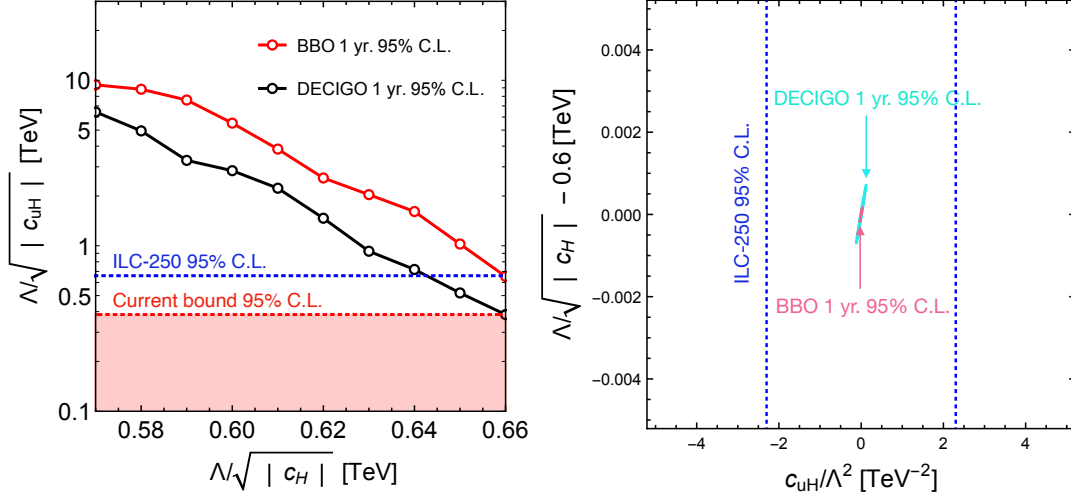


Figure 8. Left panel: Sensitivity reach of the DECIGO (black) and BBO (red) experiments to $\Lambda/\sqrt{|c_{uH}|}$ as a function of the central value of $\Lambda/\sqrt{|c_H|}$, assuming $v_b = 0.3$, the central value of $c_{uH}/\Lambda^2 = 0$, and $T_{\text{obs}} = 1$ -year statistics. The vertical axis of the left panel is not the central value of $\Lambda/\sqrt{|c_{uH}|}$, but the magnitude of 95% confidence intervals of $\Lambda/\sqrt{|c_{uH}|}$. The red-dotted line is the current bound at 95% C.L. [68]. The dashed blue line shows a sensitivity reach of the ILC-250 at 95% C.L. [66, 67]. Right panel: 95% C.L. confidence regions for DECIGO (blue-shaded) and BBO (red-shaded) with 1-year statistics, assuming the central values of $c_{uH}/\Lambda^2 = 0$ and $\Lambda/\sqrt{|c_H|} = 0.60$ TeV. The confidence interval for c_{uH}/Λ^2 direction in the right panel corresponds to one of the points in the left panel.

the SFO-EWPT that can produce the GWs; see Figs. 1-4. We numerically evaluated the sensitivity of the future GW observations to (ii) and (iii) by performing the Fisher matrix analysis. Finally, the sensitivity of the future GW observations to (ii) and (iii) was compared with that of the future collider experiments.

The results are collected in Figs. 5-10. We found that the DECIGO and the BBO experiments can be sensitive to (ii) and (iii) once the SFO-EWPT arises from (i). In particular, its sensitivities to the operators \mathcal{O}_{uH} and $\mathcal{O}_{H\Box}$ are potentially higher than future collider experiments. When the central value of C_H is determined from the collider experiments, future GW observations potentially measure the SMEFT Wilson coefficients with high precision and yield constraints on the SMEFT complementary to future collider experiments.

A Sensitivity reach of DECIGO at different bench mark point of bubble wall velocity

In Figs. 11-13, the results of DECIGO with $T_{\text{obs}} = 1$ -year statistics are shown in the case that the benchmark point of the bubble wall velocity is 0.3, and 0.5. Figs. 11-13 show that the GW spectrum increases as the bubble wall velocity increases.

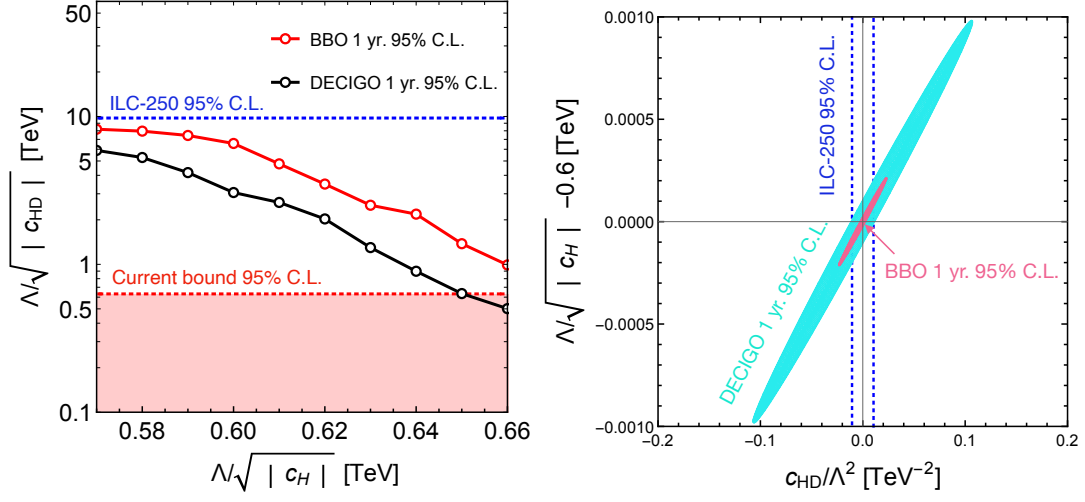


Figure 9. The same plots as Fig. 8 but for c_{HD}/Λ^2 .

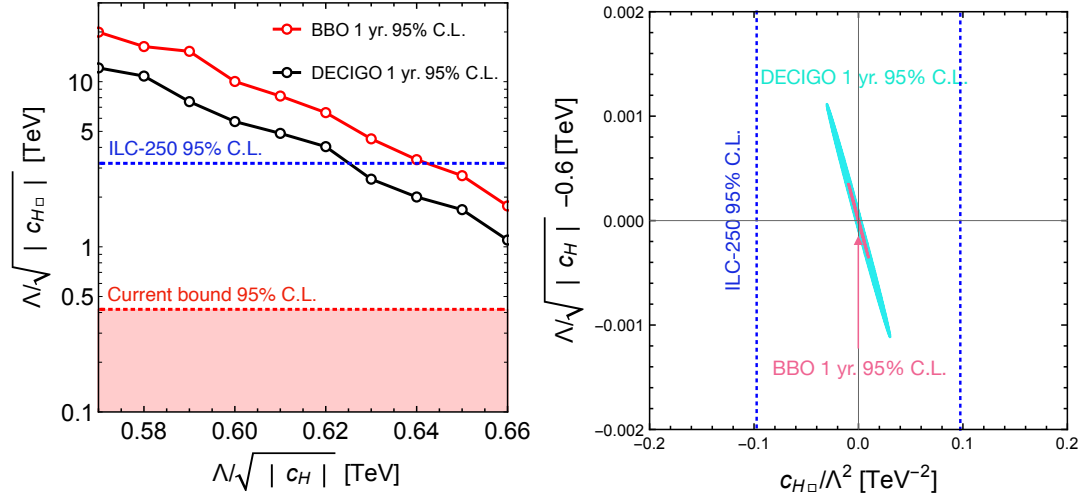


Figure 10. The same plots as Fig. 8 but for $c_{H\Box}/\Lambda^2$.

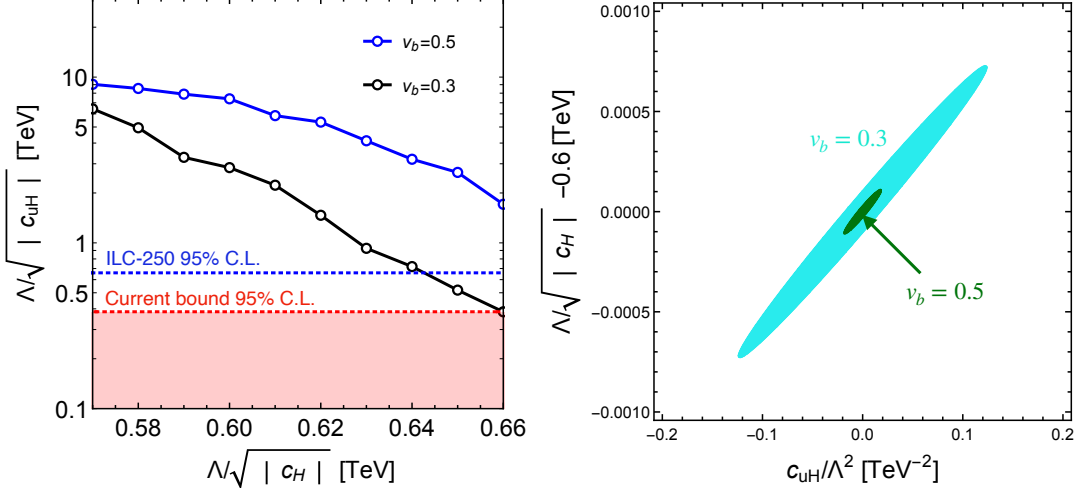


Figure 11. Left panel: Sensitivity reach of DECIGO with $T_{\text{obs}} = 1$ -year statistics to $\Lambda/\sqrt{|c_{uH}|}$ as a function of the central value of $\Lambda/\sqrt{|c_H|}$, assuming the central value of $c_{uH} = 0$. The black and blue curves represent $v_b = 0.3$ and 0.5 , respectively. Each point denotes the magnitude of confidence intervals of $\Lambda/\sqrt{|c_{uH}|}$ at 95 % C.L. ,i.e., $\delta\chi^2 = 6.0$, depending on the central values of $\Lambda/\sqrt{|c_H|}$. The dotted red line is the current bound at 95% C.L. [68]. The dashed blue line shows a sensitivity reach of the ILC-250 at 95% C.L. [66, 67]. Right panel: 95% C.L. confidence regions for DECIGO with $T_{\text{obs}} = 1$ -year statistics for $v_b = 0.3$ (shaded blue) and 0.5 (shaded green), assuming the central values of $c_{uH}/\Lambda^2 = 0$ and $\Lambda/\sqrt{|c_H|} = 0.60$ TeV. The confidence intervals for c_{uH}/Λ^2 direction in the right panel correspond to one of points in the left panel.

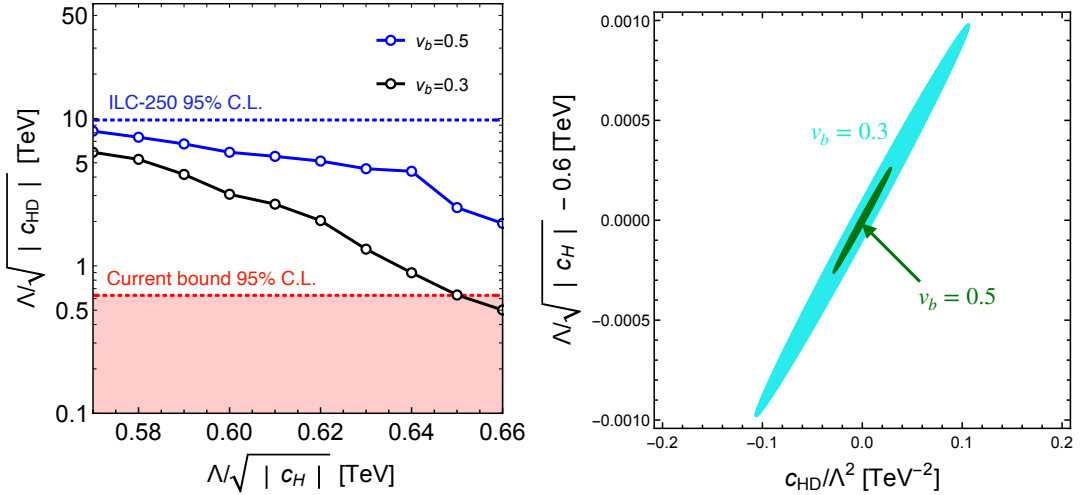


Figure 12. The same plots as Fig. 11 but for c_{HD}/Λ^2 .

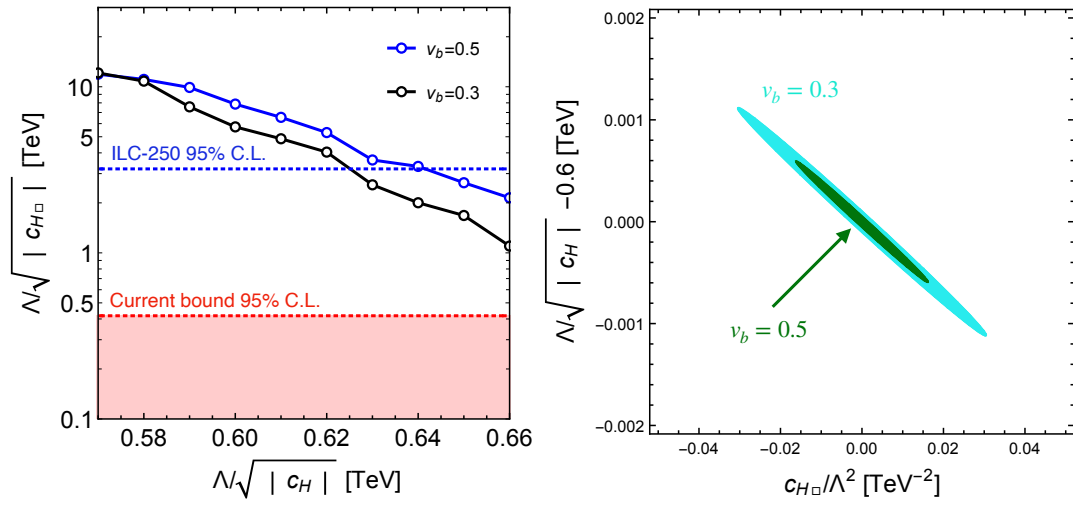


Figure 13. The same plots as Fig. 11 but for $c_{H\Box}/\Lambda^2$.

References

- [1] **ATLAS** Collaboration, G. Aad et al., *Observation of a new particle in the search for the Standard Model Higgs boson with the ATLAS detector at the LHC*, *Phys. Lett. B* **716** (2012) 1–29, [[arXiv:1207.7214](#)].
- [2] **CMS** Collaboration, S. Chatrchyan et al., *Observation of a New Boson at a Mass of 125 GeV with the CMS Experiment at the LHC*, *Phys. Lett. B* **716** (2012) 30–61, [[arXiv:1207.7235](#)].
- [3] M. B. Gavela, P. Hernandez, J. Orloff, and O. Pene, *Standard model CP violation and baryon asymmetry*, *Mod. Phys. Lett. A* **9** (1994) 795–810, [[hep-ph/9312215](#)].
- [4] T. Konstandin, T. Prokopec, and M. G. Schmidt, *Axial currents from CKM matrix CP violation and electroweak baryogenesis*, *Nucl. Phys. B* **679** (2004) 246–260, [[hep-ph/0309291](#)].
- [5] V. A. Kuzmin, V. A. Rubakov, and M. E. Shaposhnikov, *On the Anomalous Electroweak Baryon Number Nonconservation in the Early Universe*, *Phys. Lett. B* **155** (1985) 36.
- [6] K. Kajantie, M. Laine, K. Rummukainen, and M. E. Shaposhnikov, *The Electroweak phase transition: A Nonperturbative analysis*, *Nucl. Phys. B* **466** (1996) 189–258, [[hep-lat/9510020](#)].
- [7] K. Kajantie, M. Laine, K. Rummukainen, and M. E. Shaposhnikov, *Is there a hot electroweak phase transition at $m_H \gtrsim m_W$?*, *Phys. Rev. Lett.* **77** (1996) 2887–2890, [[hep-ph/9605288](#)].
- [8] K. Kajantie, M. Laine, K. Rummukainen, and M. E. Shaposhnikov, *A Nonperturbative analysis of the finite T phase transition in $SU(2) \times U(1)$ electroweak theory*, *Nucl. Phys. B* **493** (1997) 413–438, [[hep-lat/9612006](#)].
- [9] F. Csikor, Z. Fodor, and J. Heitger, *Endpoint of the hot electroweak phase transition*, *Phys. Rev. Lett.* **82** (1999) 21–24, [[hep-ph/9809291](#)].
- [10] M. D’Onofrio and K. Rummukainen, *Standard model cross-over on the lattice*, *Phys. Rev. D* **93** (2016), no. 2 025003, [[arXiv:1508.07161](#)].
- [11] **Particle Data Group** Collaboration, R. L. Workman and Others, *Review of Particle Physics*, *PTEP* **2022** (2022) 083C01.
- [12] B. Grzadkowski, M. Iskrzynski, M. Misiak, and J. Rosiek, *Dimension-Six Terms in the Standard Model Lagrangian*, *JHEP* **10** (2010) 085, [[arXiv:1008.4884](#)].
- [13] E. E. Jenkins, A. V. Manohar, and M. Trott, *Renormalization Group Evolution of the Standard Model Dimension Six Operators I: Formalism and λ Dependence*, *JHEP* **10** (2013) 087, [[arXiv:1308.2627](#)].
- [14] E. E. Jenkins, A. V. Manohar, and M. Trott, *Renormalization Group Evolution of the Standard Model Dimension Six Operators II: Yukawa Dependence*, *JHEP* **01** (2014) 035, [[arXiv:1310.4838](#)].
- [15] R. Alonso, E. E. Jenkins, A. V. Manohar, and M. Trott, *Renormalization Group Evolution of the Standard Model Dimension Six Operators III: Gauge Coupling Dependence and Phenomenology*, *JHEP* **04** (2014) 159, [[arXiv:1312.2014](#)].
- [16] C. Grojean, G. Servant, and J. D. Wells, *First-order electroweak phase transition in the standard model with a low cutoff*, *Phys. Rev. D* **71** (2005) 036001, [[hep-ph/0407019](#)].
- [17] X.-m. Zhang, *Operators analysis for Higgs potential and cosmological bound on Higgs mass*, *Phys. Rev. D* **47** (1993) 3065–3067, [[hep-ph/9301277](#)].

- [18] D. Bodeker, L. Fromme, S. J. Huber, and M. Seniuch, *The Baryon asymmetry in the standard model with a low cut-off*, *JHEP* **02** (2005) 026, [[hep-ph/0412366](#)].
- [19] S. J. Huber and T. Konstandin, *Production of gravitational waves in the nMSSM*, *JCAP* **05** (2008) 017, [[arXiv:0709.2091](#)].
- [20] C. Delaunay, C. Grojean, and J. D. Wells, *Dynamics of Non-renormalizable Electroweak Symmetry Breaking*, *JHEP* **04** (2008) 029, [[arXiv:0711.2511](#)].
- [21] S. J. Huber and M. Sopena, *An efficient approach to electroweak bubble velocities*, [arXiv:1302.1044](#).
- [22] T. Konstandin, G. Nardini, and I. Rues, *From Boltzmann equations to steady wall velocities*, *JCAP* **09** (2014) 028, [[arXiv:1407.3132](#)].
- [23] P. H. Damgaard, A. Haarr, D. O’Connell, and A. Tranberg, *Effective Field Theory and Electroweak Baryogenesis in the Singlet-Extended Standard Model*, *JHEP* **02** (2016) 107, [[arXiv:1512.01963](#)].
- [24] C. P. D. Harman and S. J. Huber, *Does zero temperature decide on the nature of the electroweak phase transition?*, *JHEP* **06** (2016) 005, [[arXiv:1512.05611](#)].
- [25] C. Balazs, G. White, and J. Yue, *Effective field theory, electric dipole moments and electroweak baryogenesis*, *JHEP* **03** (2017) 030, [[arXiv:1612.01270](#)].
- [26] J. de Vries, M. Postma, J. van de Vis, and G. White, *Electroweak Baryogenesis and the Standard Model Effective Field Theory*, *JHEP* **01** (2018) 089, [[arXiv:1710.04061](#)].
- [27] R.-G. Cai, M. Sasaki, and S.-J. Wang, *The gravitational waves from the first-order phase transition with a dimension-six operator*, *JCAP* **08** (2017) 004, [[arXiv:1707.03001](#)].
- [28] M. Chala, C. Krause, and G. Nardini, *Signals of the electroweak phase transition at colliders and gravitational wave observatories*, *JHEP* **07** (2018) 062, [[arXiv:1802.02168](#)].
- [29] G. C. Dorsch, S. J. Huber, and T. Konstandin, *Bubble wall velocities in the Standard Model and beyond*, *JCAP* **12** (2018) 034, [[arXiv:1809.04907](#)].
- [30] J. De Vries, M. Postma, and J. van de Vis, *The role of leptons in electroweak baryogenesis*, *JHEP* **04** (2019) 024, [[arXiv:1811.11104](#)].
- [31] M. Chala, V. V. Khoze, M. Spannowsky, and P. Waite, *Mapping the shape of the scalar potential with gravitational waves*, *Int. J. Mod. Phys. A* **34** (2019), no. 33 1950223, [[arXiv:1905.00911](#)].
- [32] S. A. R. Ellis, S. Ipek, and G. White, *Electroweak Baryogenesis from Temperature-Varying Couplings*, *JHEP* **08** (2019) 002, [[arXiv:1905.11994](#)].
- [33] R. Zhou, L. Bian, and H.-K. Guo, *Connecting the electroweak sphaleron with gravitational waves*, *Phys. Rev. D* **101** (2020), no. 9 091903, [[arXiv:1910.00234](#)].
- [34] S. Kanemura and M. Tanaka, *Higgs boson coupling as a probe of the sphaleron property*, *Phys. Lett. B* **809** (2020) 135711, [[arXiv:2005.05250](#)].
- [35] V. Q. Phong, P. H. Khiem, N. P. D. Loc, and H. N. Long, *Sphaleron in the first-order electroweak phase transition with the dimension-six Higgs field operator*, *Phys. Rev. D* **101** (2020), no. 11 116010, [[arXiv:2003.09625](#)].
- [36] X. Wang, F. P. Huang, and X. Zhang, *Bubble wall velocity beyond leading-log approximation in electroweak phase transition*, [arXiv:2011.12903](#).

- [37] X. Wang, F. P. Huang, and X. Zhang, *Phase transition dynamics and gravitational wave spectra of strong first-order phase transition in supercooled universe*, *JCAP* **05** (2020) 045, [[arXiv:2003.08892](#)].
- [38] S. Kanemura and R. Nagai, *A new Higgs effective field theory and the new no-lose theorem*, *JHEP* **03** (2022) 194, [[arXiv:2111.12585](#)].
- [39] M. Lewicki, M. Merchand, and M. Zych, *Electroweak bubble wall expansion: gravitational waves and baryogenesis in Standard Model-like thermal plasma*, *JHEP* **02** (2022) 017, [[arXiv:2111.02393](#)].
- [40] K. Hashino, S. Kanemura, and T. Takahashi, *Primordial black holes as a probe of strongly first-order electroweak phase transition*, *Phys. Lett. B* **833** (2022) 137261, [[arXiv:2111.13099](#)].
- [41] S. Kanemura, R. Nagai, and M. Tanaka, *Electroweak phase transition in the nearly aligned Higgs effective field theory*, *JHEP* **06** (2022) 027, [[arXiv:2202.12774](#)].
- [42] Anisha, L. Biermann, C. Englert, and M. Mühlleitner, *Two Higgs doublets, effective interactions and a strong first-order electroweak phase transition*, *JHEP* **08** (2022) 091, [[arXiv:2204.06966](#)].
- [43] M. Postma and G. White, *Cosmological phase transitions: is effective field theory just a toy?*, *JHEP* **03** (2021) 280, [[arXiv:2012.03953](#)].
- [44] S. J. Huber, M. Pospelov, and A. Ritz, *Electric dipole moment constraints on minimal electroweak baryogenesis*, *Phys. Rev. D* **75** (2007) 036006, [[hep-ph/0610003](#)].
- [45] M. Cepeda et al., *Report from Working Group 2: Higgs Physics at the HL-LHC and HE-LHC*, *CERN Yellow Rep. Monogr.* **7** (2019) 221–584, [[arXiv:1902.00134](#)].
- [46] **LCC Physics Working Group** Collaboration, K. Fujii et al., *Tests of the Standard Model at the International Linear Collider*, [arXiv:1908.11299](#).
- [47] **CLIC** Collaboration, J. de Blas et al., *The CLIC Potential for New Physics*, [arXiv:1812.02093](#).
- [48] **FCC** Collaboration, A. Abada et al., *FCC Physics Opportunities: Future Circular Collider Conceptual Design Report Volume 1*, *Eur. Phys. J. C* **79** (2019), no. 6 474.
- [49] F. An et al., *Precision Higgs physics at the CEPC*, *Chin. Phys. C* **43** (2019), no. 4 043002, [[arXiv:1810.09037](#)].
- [50] **LISA** Collaboration, P. Amaro-Seoane et al., *Laser Interferometer Space Antenna*, [arXiv:1702.00786](#).
- [51] N. Seto, *Correlation analysis of stochastic gravitational wave background around 0.1–1 Hz*, *Phys. Rev. D* **73** (2006) 063001, [[gr-qc/0510067](#)].
- [52] E. S. P. et al. *The big bang observer: Direct detection of gravitational waves from the birth of the universe to the present*, *NASA Mission Concept Study* (2004).
- [53] K. Hashino, R. Jinno, M. Kakizaki, S. Kanemura, T. Takahashi, and M. Takimoto, *Selecting models of first-order phase transitions using the synergy between collider and gravitational-wave experiments*, *Phys. Rev. D* **99** (2019), no. 7 075011, [[arXiv:1809.04994](#)].
- [54] S. A. R. Ellis, J. Quevillon, P. N. H. Vuong, T. You, and Z. Zhang, *The Fermionic Universal One-Loop Effective Action*, *JHEP* **11** (2020) 078, [[arXiv:2006.16260](#)].
- [55] S. R. Coleman and E. J. Weinberg, *Radiative Corrections as the Origin of Spontaneous Symmetry Breaking*, *Phys. Rev. D* **7** (1973) 1888–1910.
- [56] L. Dolan and R. Jackiw, *Symmetry behavior at finite temperature*, *Phys. Rev. D* **9** (Jun, 1974) 3320–3341.

- [57] M. E. Carrington, *Effective potential at finite temperature in the standard model*, *Phys. Rev. D* **45** (Apr, 1992) 2933–2944.
- [58] J. Ellis, M. Lewicki, and J. M. No, *On the Maximal Strength of a First-Order Electroweak Phase Transition and its Gravitational Wave Signal*, *JCAP* **04** (2019) 003, [[arXiv:1809.08242](#)].
- [59] A. Masoumi, K. D. Olum, and B. Shlaer, *Efficient numerical solution to vacuum decay with many fields*, *JCAP* **01** (2017) 051, [[arXiv:1610.06594](#)].
- [60] C. Caprini et al., *Detecting gravitational waves from cosmological phase transitions with LISA: an update*, *JCAP* **03** (2020) 024, [[arXiv:1910.13125](#)].
- [61] M. Hindmarsh, S. J. Huber, K. Rummukainen, and D. J. Weir, *Shape of the acoustic gravitational wave power spectrum from a first order phase transition*, *Phys. Rev. D* **96** (2017), no. 10 103520, [[arXiv:1704.05871](#)]. [Erratum: *Phys.Rev.D* 101, 089902 (2020)].
- [62] M. Hindmarsh, S. J. Huber, K. Rummukainen, and D. J. Weir, *Erratum: Shape of the acoustic gravitational wave power spectrum from a first order phase transition [phys. rev. d 96, 103520 (2017)]*, *Phys. Rev. D* **101** (Apr, 2020) 089902.
- [63] J. R. Espinosa, T. Konstandin, J. M. No, and G. Servant, *Energy Budget of Cosmological First-order Phase Transitions*, *JCAP* **06** (2010) 028, [[arXiv:1004.4187](#)].
- [64] K. Yagi and N. Seto, *Detector configuration of DECIGO/BBO and identification of cosmological neutron-star binaries*, *Phys. Rev. D* **83** (2011) 044011, [[arXiv:1101.3940](#)]. [Erratum: *Phys.Rev.D* 95, 109901 (2017)].
- [65] A. Klein et al., *Science with the space-based interferometer eLISA: Supermassive black hole binaries*, *Phys. Rev. D* **93** (2016), no. 2 024003, [[arXiv:1511.05581](#)].
- [66] J. De Blas, G. Durieux, C. Grojean, J. Gu, and A. Paul, *On the future of Higgs, electroweak and diboson measurements at lepton colliders*, *JHEP* **12** (2019) 117, [[arXiv:1907.04311](#)].
- [67] J. de Blas, Y. Du, C. Grojean, J. Gu, V. Miralles, M. E. Peskin, J. Tian, M. Vos, and E. Vryonidou, *Global SMEFT Fits at Future Colliders*, in *2022 Snowmass Summer Study*, 6, 2022. [arXiv:2206.08326](#).
- [68] **SMEFT** Collaboration, J. J. Ethier, G. Magni, F. Maltoni, L. Mantani, E. R. Nocera, J. Rojo, E. Slade, E. Vryonidou, and C. Zhang, *Combined SMEFT interpretation of Higgs, diboson, and top quark data from the LHC*, *JHEP* **11** (2021) 089, [[arXiv:2105.00006](#)].